Microphysical **A**erosol **P**roperties from **P**olarimetry (MAPP)
Algorithm **T**heoretical **B**asis **D**ocument (ATBD)

Snorre Stamnes[1]*, Michael Jones[1,2], Adam Bell[1,2], Eduard Chemyakin[1,2]
Joseph Schlosser[1], Nathan Dostart[1], Yongxiang Hu[1], Brian Cairns[3]

[1]*NASA Langley Research Center,*
Hampton, VA

[2]*Science Systems and Applications, Inc.,*
Hampton, VA

[3]*NASA Goddard Institute for Space Studies,*
New York, NY

May 10, 2023

*email: snorre.a.stamnes@nasa.gov

Contents

1 Introduction

The Microphysical Aerosol Properties from Polarimetry (MAPP) remote sensing retrieval algorithm is used to *retrieve* aerosol and ocean retrieval products from airborne and spaceborne multi-angle, multi-channel polarimetric sensors. MAPP has been applied to the following polarimeter instruments: The NASA Research Scanning Polarimeter (RSP), SPEXone and Hyper-Angular Rainbow Polarimeter #2 (HARP2) onboard the NASA Plankton, Aerosol, Cloud, ocean Ecosystem (PACE) mission, and PolCube.

For example, for PolCube, the inputs of the MAPP algorithm are the Level-1 (L1) PolCube polarimeter measurements (and their corresponding uncertainties) of the total radiance and the degree of linear polarization at three visible bands at 410, 555, 670 nm and one near-infrared band at 864 nm, which are contained with the PolCube PACE Level-1C (L1C) data.

The outputs of the MAPP algorithm are the retrieved atmospheric and ocean state parameters, *i.e.* Level-2 (L2) aerosol and ocean retrieval products, the aerosol optical and microphysical properties over the ocean including the fine-mode, sea-salt, and dust aerosol optical depth (AOD); the fine-mode, sea-salt, and dust effective radius and variance; and the fine-mode single-scattering albedo (SSA).

A unique feature of MAPP is the focus on coupled retrievals of aerosol microphysical properties and ocean color parameters using optimal estimation with vector radiative transfer and Lorenz-Mie calculations. MAPP can use neural network models for vector radiative transfer (VRT) computations or use on-the-fly VRT computations which can be advantageous for aircraft platforms where the sensor altitude and the aerosol location (top height, layering, etc.) vary. MAPP also uses accurate, pre-computed Lorenz-Mie inherent optical property (IOP) look-up-tables (LUTs). Over 90% of the signal measured by a spectroradiometer or polarimeter is due to the molecular and aerosol scattering in the atmosphere and the Fresnel reflection of the ocean surface, so that less than 10% of the signal is due to subsurface ocean inherent optical properties (particulate and dissolved matter) (Gordon, 1997). Polarimeter measurements of the polarized reflectance at multiple angles can lead to improved retrievals of underwater properties by enabling accurate characterization of the aerosol signal through retrieval of AOD, microphysical aerosol properties, including aerosol effective radius, SSA, and the real refractive index. Another advantage of polarimeters like RSP is that they do not saturate in sunglint, which is a significant issue for instruments like MODIS.

The methodology of the MAPP algorithm is described in Section 2, and is summarized by using optimal estimation theory to invert the polarimetric measurements in order to obtain the retrieval parameters, which determine the state of the atmosphere (aerosol) and ocean models. In Section 2.1, we present this retrieval framework based on principles of optimal estimation, while Section 2.2 includes descriptions of the polarimetric sensors to which MAPP has been applied. Section 3 discusses pixel masking including the highly important topic of cloud masks. Section 4 summarizes the MAPP L2 output format specification and products with a table providing a list of all products. Section 5 provides a user manual describing how to run the MAPP algorithm. Section 6 describes the polarimetric uncertainty models used in MAPP. Section 7 provides details on the product uncertainty calculations.

The RSP MAPP products are also summarized on the NASA LaRC polarimeter website (https://science.larc.nasa.gov/polarimetry) (Stamnes et al.) and are available for download

at the NASA GISS RSP website (https://data.giss.nasa.gov/pub/rsp) (Cairns et al.).

2 The MAPP algorithm

In this section, we describe our overall methodology, which involves formulating the inverse problem for observations from a polarimetric sensor. We use optimal estimation theory to formulate this inverse problem such that we have a forward model that goes from the input atmospheric/aerosol/oceanic/land state to the output observations measured by the polarimetric sensor. An iteration is performed such that the input is changed until the modeled output measurements from this "forward model" fit the observations to within the measurement uncertainties of the polarimetric sensor.

In Section 2.1, we present this retrieval framework based on principles of optimal estimation, while Section 2.2 includes descriptions of the polarimetric sensors to which MAPP has been applied. The forward models are described in Section 2.3. The neural network forward models are described in Section 2.4. The aerosol and cloud models are described in Section 2.5. The atmosphere models are described in Section 2.6. The ocean and land surface reflectance models are described in Section 2.7.

The MAPP algorithm can be used to develop new polarimeter instruments through the generation of user-customized simulated polarimeter data for an arbitrary number of wavelengths, viewing zenith angles, Stokes parameters, and instrument-solar geometries. MAPP can be used to perform retrievals on such synthetic datasets to quantify and optimize the polarimeter's performance for a given geophysical variable. MAPP can also be used to test the performance of different forward models (atmospheric and ocean/land) state parameters for a given polarimeter instrument. MAPP can also be used to quantify the performance of existing polarimeter instruments. For example, we can generate simulated data for the seven RSP window channels at $\lambda = 410$, 469, 555, 670, 864, 1594, and 2264 nm, and add noise as discussed in Section 6. (The complete list of RSP channels is described in Section 2.2. For RSP, the 960 nm channel to determine the water vapor absorption using Eq. (26).)

A detailed description of the MAPP algorithm is given in Stamnes et al. (2018), where it is applied to the RSP (Cairns et al., 1999). A description of MAPP applied to PolCube is given in (Stamnes et al., 2021). A detailed description of MAPP applied to the SPEXone and HARP2 polarimeters onboard the future PACE mission is given in (Stamnes et al., 2023). We start with a description of the MAPP optimal estimation algorithm for polarimeter instruments. A flow chart of of the MAPP algorithm for PACE is provided in Fig.1.

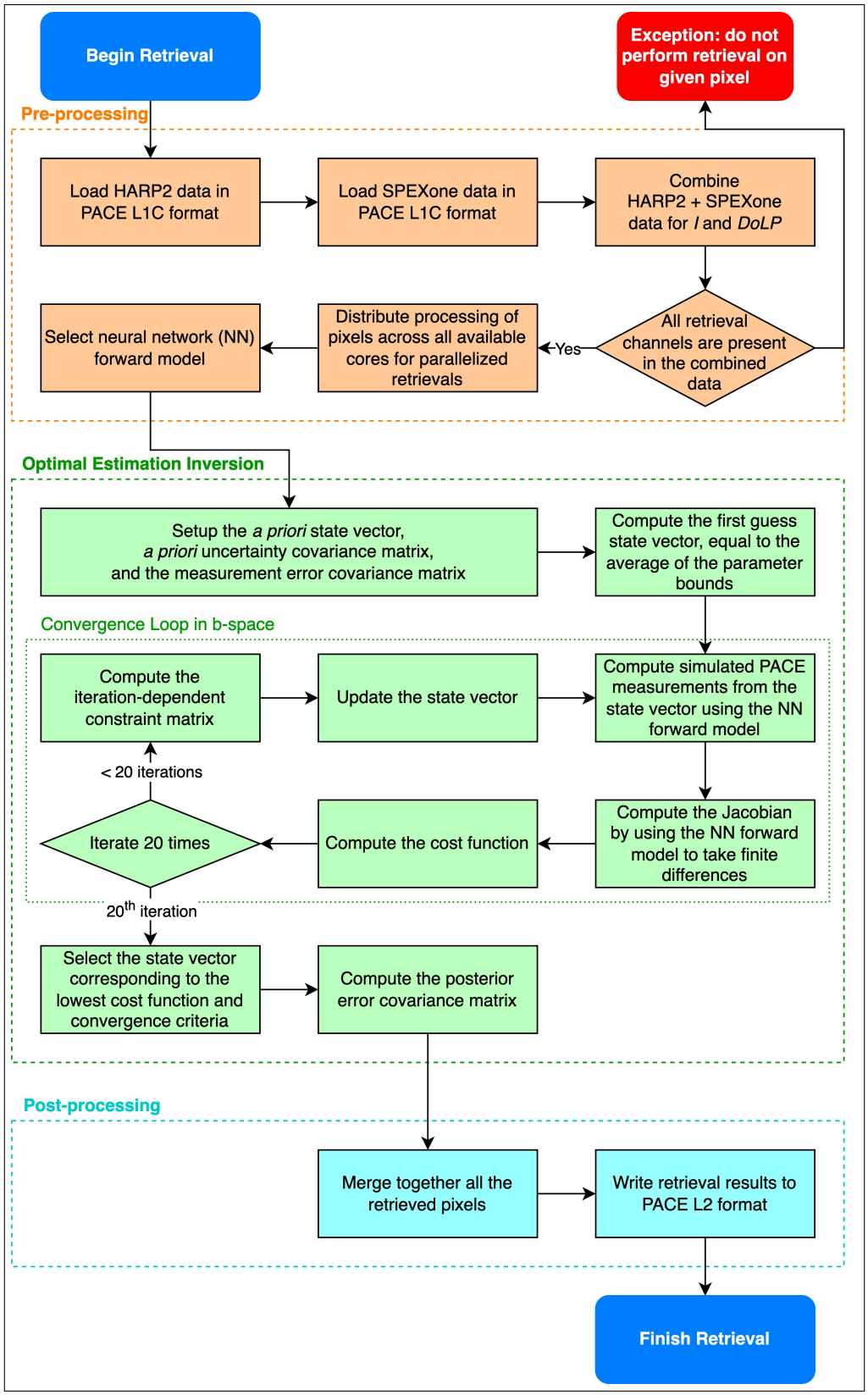

Figure 1: MAPP flow chart of retrieval methodology including the pre-processing, optimal estimation inversion, and post-processing procedures. This example is specifically for the PACE polarimeters but the procedure is similar for RSP and PolCube.

2.1 Optimal estimation

The optimal estimation method used in MAPP has its heritage from a method used for inverting atmospheric temperature and water vapor vertical profiles, cloud, and surface properties from hyperspectral infrared sounders (Wu et al., 2017). For retrievals performed on both real and simulated polarimeter data, this method is found to be reliable and efficient in terms of the number of forward model evaluations required to achieve convergence.

2.1.1 State vector

The state vector of MAPP retrieval parameters for observations of aerosols over the ocean can be defined as follows:

$$\mathbf{x} = \langle \tau_{556f} \;\; r_{nf} \;\; n_{rf} \;\; n_{if} \; \tau_{556c} \;\; r_{nc} \;\; \sigma_{gf} \;\; \sigma_{gc} \;\; z_{FTL} \;\; v \;\; [\text{Chla}] \;\; n_{rc} \;\; r_{nd} \;\; \tau_{556d} \rangle$$

where the labels f, c, and d denote fine-mode aerosol, coarse-mode sea salt aerosol, and coarse-mode dust aerosol, respectively. The aerosol size distributions are assumed to be lognormal. τ_{556} is the optical depth at the wavelength 556 nm. n_r and n_i are respectively the real and imaginary refractive indices. r_n is the median radius. σ_g is the size distribution width. The ocean surface roughness is described by the windspeed v [m/s] and the subsurface absorption and scattering is parameterized in terms of the chlorophyll concentration Chla [mg/m^3] with details provided in Section 2.7.1. τ_{555f} is the fine (accumulation) mode AOD at 556 nm, r_{nf} is the number-density mean radius with geometric width σ_{gf}, $n_{rf} + in_{if}$ is the fine-mode refractive index (assumed to be spectrally invariant), τ_{556c} is the AOD of the coarse mode, r_{nc} is the coarse mode number-density mean radius with geometric width σ_{gc}. The coarse mode refractive index, $n_{rc} + in_{ic}$, is assumed *a priori* to be equal to that of water to represent hydrated sea salt (marine) aerosols and to be assumed from climatology for non-spherical dust particles (see Section 2.5.1). The ranges allowed for each of the parameters in this 14-parameter retrieval are provided in Table 1, where the numbered parameters comprise the state vector. Parameters 1-11 are included in the bimodal aerosol ocean retrieval that incorporates fine-mode aerosol mixed with coarse-mode sea salt aerosol. Parameters 1-14 are used in the trimodal aerosol retrieval that adds non-spherical dust aerosols mixed into the free tropospheric layer (FTL). A detailed description of the aerosol model and how aerosol location handled are discussed in Section 2.5.1.

2.1.2 Cost function

The cost function is defined as Rodgers (2000)

$$\begin{aligned} \chi^2(\mathbf{x}) &= \Phi(\mathbf{x}) \\ &= \Phi(\mathbf{x})_{\text{data}} + \Phi(\mathbf{x})_{\text{prior}} \\ &= \frac{1}{2}(\boldsymbol{f} - \mathbf{y})^T \mathbf{S}_\epsilon^{-1}(\boldsymbol{f} - \mathbf{y}) + \frac{1}{2}(\mathbf{x} - \mathbf{x}_a)^T \mathbf{S}_a^{-1}(\mathbf{x} - \mathbf{x}_a). \end{aligned} \tag{1}$$

The vector radiative transfer model, described in Section 2.3, is our forward model, providing R_{I_L}, R_{I_R} and DoLP, represented by $\boldsymbol{f}$, which are a function of the state vector $\mathbf{x}$, Eq. (1), and which provide a suitable model for the measured R_{I_L}, R_{I_R} and DoLP, represented by

Table 1: MAPP aerosol and ocean retrieval parameters and ranges.

No.	Parameter [Unit]	Min	Max
1.	τ_{556f}	1e-5	0.7
2.	τ_{556c}	1e-5	0.3
3.	n_{rf}	1.39	1.65
4.	n_{if}	1e-5	0.045
5.	r_{nf} [μm]	0.075	0.15
6.	r_{nc} [μm]	0.5	1.5
7.	σ_{gf}	ln(1.4)	ln(2.01)
8.	σ_{gc}	ln(1.35)	ln(2.01)
9.	FTL base height [km]	1.01	7.0
10.	v [m/s]	1.0	13.0
11.	Chla [mg/m^3]	0.01	9.0
	$r_{eff,f}$ [μm]	0.10	0.51
	$v_{eff,f}$	0.12	0.62
	$r_{eff,c}$ [μm]	0.63	5.07
	$v_{eff,c}$	0.09	0.62
12.	n_{rc}	1.333	1.366
13.	r_{nd} [μm]	0.6	1.5
14.	τ_{556d}	0	0.2
	$\sigma_{gd} \equiv \sigma_{gc}$		
	$r_{eff,d}$ [μm]	0.75	5.07
	$v_{eff,d}$	0.09	0.62

$\mathbf{y}$ (either real measurements from RSP or synthetic measurements generated by the forward model with noise added). The first term may be called the *data* term since it depends on residuals of the forward model and the measurement, taking into account measurement error through its covariance matrix $\mathbf{S}_\epsilon$. The second term may be considered the *a priori* term since it is the departure of the state vector $\mathbf{x}$ from the *a priori* state vector $\mathbf{x}_a$, with *a priori* uncertainty provided by the covariance matrix $\mathbf{S}_a$. The *a priori* state vector and covariance matrices for our problem are defined below. It is convenient to define the *normalized* cost function of the data term by dividing by the number of measurements, m:

$$\begin{aligned}\chi' &= \frac{1}{m}\sqrt{\Phi(\mathbf{x})_{\text{data}}} \\ &= \frac{1}{m}\sqrt{\frac{1}{2}(\boldsymbol{f}-\mathbf{y})^T\mathbf{S}_\epsilon^{-1}(\boldsymbol{f}-\mathbf{y})}.\end{aligned} \tag{2}$$

2.1.3 Retrieval convergence criteria

Generally speaking for a successful retrieval, $\frac{1}{m}\sqrt{\Phi(\mathbf{x})} < 1$, and if there happen to be redundant measurements then $\frac{1}{m}\sqrt{\Phi(\mathbf{x})} \ll 1$. For inversions of real RSP data, we consider retrievals successful if $\chi' < 0.1$.

2.1.4 Transformations

A transformation into **b**-space is used to smooth out changes between the different state parameters that have different units and ranges, which is similar to a transformation into log-space (Stamnes et al., 2018). First, the state vector $\mathbf{x}$ is transformed into fifth-root-space $\mathbf{x_1}$ to smooth changes in the state parameters, analogous to a transformation into log-space:

$$\mathbf{x_1} = \mathbf{x}^{1/5}. \tag{3}$$

In order to ensure that the state vector does not go out-of-bounds, described by $\mathbf{x}^{\text{low}}$ and $\mathbf{x}^{\text{high}}$ using the ranges of the state vector following Eq. (1), we found that the following transformation to **b**-space works well:

$$\mathbf{b} = \log \frac{\mathbf{x_1} - \mathbf{x_1}^{\text{low}}}{\mathbf{x_1}^{\text{high}} - \mathbf{x_1}}. \tag{4}$$

If $\mathbf{x}$ is out-of-bounds the argument of the log will be negative, and will evaluate to an imaginary number. In order to transform from **b**-space to $\mathbf{x_1}$-space we can use the transformation:

$$\mathbf{x_1} = \frac{\mathbf{x_1}^{\text{high}}}{1 + e^{-\mathbf{b}}} + \frac{\mathbf{x_1}^{\text{low}}}{1 + e^{\mathbf{b}}}. \tag{5}$$

Then $\mathbf{x}$ is given by $\mathbf{x} = {\mathbf{x_1}}^5$. The retrieval is performed in **b**-space. Therefore by definition, $\mathbf{x_1} \in \mathbb{R}^+$, and thus $\mathbf{x}$ will also be positive and real-valued.

2.1.5 Jacobian

The $m \times n$ Jacobian matrix $\mathbf{K} \equiv \frac{\partial}{\partial \mathbf{x}} \boldsymbol{f}$ is expressed in **b**-space by:

$$\mathbf{K_b} = \frac{d\boldsymbol{f}}{d\mathbf{b}} = \frac{d\mathbf{x}}{d\mathbf{b}} \frac{d\boldsymbol{f}}{d\mathbf{x}} = \frac{d\mathbf{x}}{d\mathbf{b}} \mathbf{K} = \frac{d\mathbf{x}}{d\mathbf{x_1}} \frac{d\mathbf{x_1}}{d\mathbf{b}} \mathbf{K}. \tag{6}$$

2.1.6 Scaled cost function

The *scaled* cost function is a scalar value χ_s^2 defined by:

$$\chi_s^2 = \frac{1}{2}(\boldsymbol{f} - \mathbf{y})^T \mathbf{S}_\epsilon^{-1} (\boldsymbol{f} - \mathbf{y}) + \frac{1}{2}(\mathbf{b} - \mathbf{b}_a)^T {\mathbf{S_1}_a}^{-1} (\mathbf{b} - \mathbf{b}_a) \tag{7}$$

where $\mathbf{b}_a$ is the *a priori* state vector in **b**-space and $\mathbf{S_1}_a$ is the *a priori* covariance in **b**-space proportional to the Jacobian.

2.1.7 Iteration

In nonlinear optimal estimation, we minimize the cost function, Eq. (1) or Eq. (7), through an iterative process whereby the state vector $\mathbf{x}$ is changed until the resulting forward-modeled measurements $\boldsymbol{f}(\mathbf{x})$ match the measurements $\mathbf{y}$ within their uncertainties, as outlined in Fig. 1. A transformation into **b**-space is used to smooth out changes between the different

state parameters that have different units and ranges. The next step in the iteration is given according to the following equation:

$$\mathbf{b}_{i+1} = \mathbf{b}_a + \mathbf{S}_i[(\boldsymbol{f} - \mathbf{y}) + \mathbf{K}_\mathbf{b}(\mathbf{b}_i - \mathbf{b}_a)] \tag{8}$$

where $\mathbf{b}_i$, $\mathbf{b}_a$, and $\mathbf{K}_\mathbf{b}$ represent in $\mathbf{b}$-space the state vector at the ith step, the *a priori* state vector, and the Jacobian matrix, respectively. $\mathbf{S}_i$ is the iteration-dependent constraint matrix Wu et al. (2017). The iteration-dependent constraint matrix $\mathbf{S}_i$ is given by:

$$\mathbf{S}_i = (\mathbf{K}_\mathbf{b}^T \Lambda_i \mathbf{S}_\epsilon^{-1} \mathbf{K}_\mathbf{b} + \mathbf{S}_{\mathbf{1}a}^{-1})^+ \tag{9}$$

where $\mathbf{S}_{\mathbf{1}a}$ is the *a priori* constraint matrix in $\mathbf{b}$-space. The symbol + denotes the pseudoinverse. The iteration-dependent damping factor

$$\Lambda_i = \frac{1}{a_0 - \frac{a_0 - 1}{1 + e^{n_0 - i}}} \tag{10}$$

has constants $a_0 = 1000$ and $n_0 = 8$ that are determined empirically such that the state vector converges to a solution in an efficient and robust manner (Wu et al., 2017).
In practice, we train a neural network to provide the output for our forward model. We take finite differences of this neural network forward model to compute the Jacobian, which we can efficiently compute by consolidating all inputs into a single call to TensorFlow per iteration as described in Section 2.4.3.

2.1.8 *A priori* covariance matrix and constraints

We use a conservative and simple way to specify the *a priori* state vector, $\mathbf{x}_a$, using the mean of the allowable range of each retrieval parameter, and which is also used as the first guess $\mathbf{x}_i$:

$$\mathbf{x}_a = (\mathbf{x}_{\text{low}} + \mathbf{x}_{\text{high}})/2 \equiv \mathbf{x}_i. \tag{11}$$

The *a priori* covariance matrix, defined as a diagonal matrix, is given by

$$\mathbf{S}_a = \text{diag}(\vec{\sigma_a} \circ \vec{\sigma_a}), \tag{12}$$

where $\vec{\sigma_a}$ is a vector representing the standard deviations of the *a priori* values, which represent 1σ uncertainties, and is set equal to the *a priori* state vector, so that $\vec{\sigma_a} = \mathbf{x}_a$ and $\vec{\sigma_a} \circ \vec{\sigma_a}$ denotes the Schur product.[1] The measurement error covariance matrix $\mathbf{S}_\epsilon$ is given in Section 6.

2.1.9 Posterior covariance matrix

Once the retrieval has converged to $\hat{\mathbf{x}}$, we calculate the posterior covariance matrix at $\hat{\mathbf{x}}$, or the state error covariance matrix, given by

$$\hat{\mathbf{S}}^{-1}(\hat{\mathbf{x}}) = \mathbf{K}(\hat{\mathbf{x}})^T \Lambda_i \mathbf{S}_\epsilon^{-1} \mathbf{K}(\hat{\mathbf{x}}) + \mathbf{S}_a^{-1}. \tag{13}$$

[1] Also known as the Hadamard product, it is simply the element-by-element product. See https://en.wikipedia.org/wiki/Hadamard_product_(matrices).

The square root of the diagonals of $\hat{\mathbf{S}}$ give the 1σ uncertainty estimates of the retrieval accuracy, and the non-diagonal elements indicate how correlated the retrieval parameters are to each other. A diagonal or nearly-diagonal $\hat{\mathbf{S}}(\hat{\mathbf{x}})$ indicates that the retrieval parameters are orthogonal to each other, without overlapping impacts on the modeled measurements. The MAPP L2 data files with the retrievals provide the uncertainty estimates corresponding to the state vector from Eq. (13). Also provided are the propagated uncertainties for the fine- and coarse-mode effective radii, effective variances, and the fine-mode SSA. For details on the propagation of errors, see Section 7.

References

Michael J Behrenfeld, Richard H Moore, Chris A Hostetler, Jason Graff, Peter Gaube, Lynn M Russell, Gao Chen, Scott C Doney, Stephen Giovannoni, Hongyu Liu, et al. The North Atlantic aerosol and marine ecosystem study (NAAMES): science motive and mission overview. *Frontiers in Marine Science*, 6, 2019.

Alexander Berk, Lawrence S Bernstein, and David C Robertson. MODTRAN: A moderate resolution model for LOWTRAN. Technical report, DTIC Document, 1987.

Brian Cairns, Edgar E Russell, and Larry D Travis. Research scanning polarimeter: calibration and ground-based measurements. In *SPIE's International Symposium on Optical Science, Engineering, and Instrumentation*, pages 186–196. International Society for Optics and Photonics, 1999.

Brian Cairns, Barbara E Carlson, Ruoxian Ying, Andrew A Lacis, and V Oinas. Atmospheric correction and its application to an analysis of hyperion data. *IEEE Transactions on Geoscience and Remote Sensing*, 41(6):1232–1245, 2003.

Brian Cairns, M Lacis Alexandrov, Barbara Carlson, et al. Inversion of multi-angle radiation measurement. Technical report, Columbia University, New York, New York; NASA Goddard Institute for Space Studies, New York, New York (US), 2005.

(Cairns et al.). NASA GISS RSP website. https://data.giss.nasa.gov/pub/rsp. Accessed: 2017-09-16.

Eduard Chemyakin, Snorre Stamnes, Sharon P. Burton, Xu Liu, Chris Hostetler, Richard Ferrare, Brian Cairns, and Oleg Dubovik. Improved Lorenz-Mie look-up table for lidar and polarimeter retrievals. *Front. Remote Sens.*, 2:711106, 2021. URL https://doi.org/10.3389/frsen.2021.711106.

Nan Chen, Wei Li, Charles Gatebe, Tomonori Tanikawa, Masahiro Hori, Rigen Shimada, Teruo Aoki, and Knut Stamnes. New neural network cloud mask algorithm based on radiative transfer simulations. *Remote Sensing of Environment*, 219:62–71, 2018.

J. Chowdhary, B. Cairns, F. Waquet, K. Knobelspiesse, M. Ottaviani, J. Redemann, L. Travis, and M. Mishchenko. Sensitivity of multiangle, multispectral polarimetric remote sensing over open oceans to water-leaving radiance: Analyses of RSP data acquired during the MILAGRO campaign. *Remote Sensing of environment*, 118:284–308, 2012.

Jacek Chowdhary, Brian Cairns, and Larry D Travis. Contribution of water-leaving radiances to multiangle, multispectral polarimetric observations over the open ocean: bio-optical model results for case 1 waters. *Applied Optics*, 45(22):5542–5567, 2006.

Jacek Chowdhary, Pengwang Zhai, Emmanuel Boss, Heidi M Dierssen, Robert J Frouin, Amir I Ibrahim, Zhongping Lee, Lorraine Ann Remer, Michael Twardowski, Feng Xu, et al. Modeling atmosphere-ocean radiative transfer: A pace mission perspective. *Frontiers in Earth Science*, 7:100, 2019.

D Cohen, S Stamnes, T Tanikawa, Endre R Sommersten, Jakob J Stamnes, Jon K Lotsberg, and K Stamnes. Comparison of discrete ordinate and monte carlo simulations of polarized radiative transfer in two coupled slabs with different refractive indices. *Optics express*, 21 (8):9592–9614, 2013.

Charles Cox and Walter Munk. Measurement of the roughness of the sea surface from photographs of the Sun's glitter. *JOSA*, 44(11):838–850, 1954.

JF De Haan, PB Bosma, and JW Hovenier. The adding method for multiple scattering calculations of polarized light. *Astronomy and astrophysics*, 183:371–391, 1987.

Oleg Dubovik, Brent Holben, Thomas F Eck, Alexander Smirnov, Yoram J Kaufman, Michael D King, Didier Tanré, and Ilya Slutsker. Variability of absorption and optical properties of key aerosol types observed in worldwide locations. *Journal of the atmospheric sciences*, 59(3):590–608, 2002.

Oleg Dubovik, Alexander Sinyuk, Tatyana Lapyonok, Brent N. Holben, Michael I. Mishchenko, Ping Yang, Thomas F. Eck, Hester Volten, Olga Muñoz, Ben Veihelmann, Wim J. van der Zande, Jean Francois Leon, Michael Sorokin, and Ilya Slutsker. Application of spheroid models to account for aerosol particle nonsphericity in remote sensing of desert dust. *J. Geophys. Res.*, 111:D11208, 2006. URL https://doi.org/10.1029/2005JD006619.

Yongzhen Fan, Wei Li, Nan Chen, Jae-Hyun Ahn, Young-Je Park, Susanne Kratzer, Thomas Schroeder, Joji Ishizaka, Ryan Chang, and Knut Stamnes. Oc-smart: A machine learning based data analysis platform for satellite ocean color sensors. *Remote Sensing of Environment*, 253:112236, 2021.

Howard R Gordon. Atmospheric correction of ocean color imagery in the Earth observing system era. *Journal of Geophysical Research: Atmospheres*, 102(D14):17081–17106, 1997.

James E Hansen. Multiple scattering of polarized light in planetary atmospheres part ii. sunlight reflected by terrestrial water clouds. *Journal of the Atmospheric Sciences*, 28(8): 1400–1426, 1971.

James E Hansen and Larry D Travis. Light scattering in planetary atmospheres. *Space Science Reviews*, 16(4):527–610, 1974.

JE Hansen and JW Hovenier. The doubling method applied to multiple scattering of polarized light. *Journal of Quantitative Spectroscopy and Radiative Transfer*, 11(6):809–812, 1971.

OP Hasekamp. Capability of multi-viewing-angle photo-polarimetric measurements for the simultaneous retrieval of aerosol and cloud properties. *Atmospheric Measurement Techniques Discussions*, 3(2):1229–1262, 2010.

Otto P Hasekamp, Guangliang Fu, Stephanie P Rusli, Lianghai Wu, Antonio Di Noia, Joost aan de Brugh, Jochen Landgraf, J Martijn Smit, Jeroen Rietjens, and Aaldert van Amerongen. Aerosol measurements by SPEXone on the NASA PACE mission: expected retrieval

capabilities. *Journal of Quantitative Spectroscopy and Radiative Transfer*, 227:170–184, 2019.

JW Hovenier. Multiple scattering of polarized light in planetary atmospheres. *Astronomy and Astrophysics*, 13:7, 1971.

Y Huot, A Morel, MS Twardowski, D Stramski, and RA Reynolds. Particle optical backscattering along a chlorophyll gradient in the upper layer of the eastern south pacific ocean. *Biogeosciences Discussions*, 4(6):4571–4604, 2007.

Minsup Jeong, Young-Jun Choi, Sungsoo S Kim, Il-Hoon Kim, Yuriy G Shkuratov, and Hongu Yang. Multi-band polarimetry of the lunar surface. ii. grain size evolutionary pathway. *The Astrophysical Journal*, 869(1):67, 2018.

Kirk D Knobelspiesse, Sean Bailey, Brian Cairns, Bryan A Franz, Joel M Gales, Meng Gao, Otto P Hasekamp, Jochen Landgraf, Jose-Vanderlei Martins, Martin A Montes, et al. Development of a common level-1c product to facilitate multi-sensor science from the nasa pace mission. In *AGU Fall Meeting Abstracts*, volume 2020, pages A091–0005, 2020.

Matthew D Lebsock, Tristan S L'Ecuyer, and Graeme L Stephens. Information content of near-infrared spaceborne multiangular polarization measurements for aerosol retrievals. *Journal of Geophysical Research: Atmospheres*, 112(D14), 2007.

JJ Michalsky, JC Liljegren, and LC Harrison. A comparison of sun photometer derivations of total column water vapor and ozone to standard measures of same at the southern great plains atmospheric radiation measurement site. *Journal of Geophysical Research-All Series-*, 100:25–995, 1995.

Michael I Mishchenko, Larry D Travis, Ralph A Kahn, and Robert A West. Modeling phase functions for dustlike tropospheric aerosols using a shape mixture of randomly oriented polydisperse spheroids. *Journal of Geophysical Research: Atmospheres*, 102(D14):16831–16847, 1997.

André Morel and Stéphane Maritorena. Bio-optical properties of oceanic waters- a reappraisal. *Journal of Geophysical research*, 106(C4):7163–7180, 2001.

Andre Morel and James L Mueller. Normalized water-leaving radiance and remote sensing reflectance: Bidirectional reflectance and other factors. *Ocean Optics Protocols for Satellite Ocean Color Sensor Validation*, 2:183–210, 2002.

Robin M Pope, Edward S Fry, et al. Absorption spectrum (380-700 nm) of pure water. II. integrating cavity measurements. *Applied Optics*, 36(33):8710–8723, 1997.

C.D. Rodgers. *Inverse methods for atmospheric sounding*. World Scientific, 2000.

Beat Schmid, Joseph J Michalsky, Donald W Slater, James C Barnard, Rangasayi N Halthore, James C Liljegren, Brent N Holben, Thomas F Eck, John M Livingston, Philip B Russell, et al. Comparison of columnar water-vapor measurements from solar transmittance methods. *Applied Optics*, 40(12):1886–1896, 2001.

Chae Kyung Sim, Sungsoo S Kim, Minsup Jeong, Young-Jun Choi, and Yuriy G Shkuratov. Observational strategy for KPLO/PolCam measurements of the lunar surface from orbit. *Publications of the Astronomical Society of the Pacific*, 132(1007):015004, 2019.

Raymond C Smith and Karen S Baker. Optical properties of the clearest natural waters (200–800 nm). *Applied Optics*, 20(2):177–184, 1981.

K. Stamnes, G. E. Thomas, and J. J. Stamnes. *Radiative transfer in the atmosphere and ocean*. Cambridge University Press, 2 edition, 2017.

S Stamnes, C Hostetler, R Ferrare, S Burton, X Liu, J Hair, Y Hu, A Wasilewski, W Martin, B van Diedenhoven, et al. Simultaneous polarimeter retrievals of microphysical aerosol and ocean color parameters from the "mapp" algorithm with comparison to high-spectral-resolution lidar aerosol and ocean products. *Applied Optics*, 57(10):2394–2413, 2018.

Snorre Stamnes, Rosemary Baize, Paula Bontempi, Brian Cairns, Eduard Chemyakin, Young-Jun Choi, Jacek Chowdhary, Yo ngxiang Hu, Minsup Jeong, Kyung-In Kang, et al. Simultaneous aerosol and ocean properties from the polcube cubesat polarimeter. *Frontiers in Remote Sensing*, 2:19, 2021.

Snorre Stamnes, Michael Jones, James George Allen, Eduard Chemyakin, Adam Bell, Jacek Chowdhary, Xu Liu, Sharon P Burton, Bastiaan Van Diedenhoven, Otto Hasekamp, et al. The pace-mapp algorithm: Simultaneous aerosol and ocean polarimeter products using coupled atmosphere-ocean vector radiative transfer. *Frontiers in Remote Sensing*, 4:34, 2023.

(Stamnes et al.). NASA Langley Polarimetry website. https://science.larc.nasa.gov/polarimetry. Accessed: 2023-05-11.

Hendrik Christoffel Van de Hulst. *A new look at multiple scattering*. NASA Institute for Space Studies, Goddard Space Flight Center, 1963.

B van Diedenhoven, B Cairns, IV Geogdzhayev, AM Fridlind, AS Ackerman, P Yang, and BA Baum. Remote sensing of ice crystal asymmetry parameter using multi-directional polarization measurements–part 1: Methodology and evaluation with simulated measurements. *Atmospheric Measurement Techniques*, 5(10):2361–2374, 2012.

B van Diedenhoven, B Cairns, AM Fridlind, AS Ackerman, and TJ Garrett. Remote sensing of ice crystal asymmetry parameter using multi-directional polarization measurements–part 2: Application to the research scanning polarimeter. *Atmospheric Chemistry and Physics*, 13(6):3185–3203, 2013.

B. van Diedenhoven, A. S. Ackerman, A. M. Fridlind, B. Cairns, and J. Riedi. Global statistics of cloud top ice microphysical and optical properties. *J. Geophys. Res. Atmos.*, 125(6):e2019JD031811, 2020. doi: 10.1029/2019JD031811.

Wan Wu, Xu Liu, Daniel K Zhou, Allen M Larar, Qiguang Yang, Susan H Kizer, and Quanhua Liu. The application of PCRTM physical retrieval methodology for IASI cloudy scene analysis. *IEEE Transactions on Geoscience and Remote Sensing*, 2017.

Ping Yang, Kuo-Nan Liou, Lei Bi, Chao Liu, Bingqi Yi, and Bryan A Baum. On the radiative properties of ice clouds: Light scattering, remote sensing, and radiation parameterization. *Advances in Atmospheric Sciences*, 32(1):32–63, 2015.